



HAL
open science

The twisted jets of Circinus X-1

M. Coriat, R. P. Fender, C. Tasse, O. Smirnov, A.K. Tzioumis, J.W. Broderick

► **To cite this version:**

M. Coriat, R. P. Fender, C. Tasse, O. Smirnov, A.K. Tzioumis, et al.. The twisted jets of Circinus X-1. *Monthly Notices of the Royal Astronomical Society*, 2019, 484 (2), pp.1672-1686. 10.1093/mnras/stz099 . hal-01999482

HAL Id: hal-01999482

<https://hal.science/hal-01999482>

Submitted on 28 Jun 2023

HAL is a multi-disciplinary open access archive for the deposit and dissemination of scientific research documents, whether they are published or not. The documents may come from teaching and research institutions in France or abroad, or from public or private research centers.

L'archive ouverte pluridisciplinaire **HAL**, est destinée au dépôt et à la diffusion de documents scientifiques de niveau recherche, publiés ou non, émanant des établissements d'enseignement et de recherche français ou étrangers, des laboratoires publics ou privés.

The twisted jets of Circinus X-1

M. Coriat¹,^{2,3}★ R. P. Fender,⁴ C. Tasse,^{5,6} O. Smirnov,^{3,6} A. K. Tzioumis⁷ and J. W. Broderick⁸

¹IRAP, Université de Toulouse, CNRS, CNES, UPS, 9 av. du colonel Roche, F-31038, Toulouse, France

²Department of Astronomy, University of Cape Town, Private Bag X3, Rondebosch 7701, South Africa

³SKA South Africa, 3rd Floor, The Park, Park Road, Pinelands 7405, South Africa

⁴Astrophysics, Department of Physics, University of Oxford, Keble Road, Oxford OX1 3RH, UK

⁵GEPI, Observatoire de Paris, CNRS, Université Paris Diderot, 5 place Jules Janssen, F-92190 Meudon, France

⁶Department of Physics & Electronics, Rhodes University, PO Box 94, Grahamstown 6140, South Africa

⁷Australia Telescope National Facility, CSIRO, PO Box 76, Epping, New south Wales 1710, Australia

⁸ASTRON, the Netherlands Institute for Radio Astronomy, Postbus 2, NL-7990 AA Dwingeloo, The Netherlands

Accepted 2019 January 7. Received 2019 January 7; in original form 2018 July 16

ABSTRACT

We present the results of millimetre (33 and 35 GHz) and centimetre (2.1, 5.5, and 9.0 GHz) wavelength observations of the neutron star X-ray binary Circinus X-1, using the Australia Telescope Compact Array. We have used advanced calibration and de-convolution algorithms to overcome multiple issues due to intrinsic variability of the source and direction-dependent effects. The resulting centimetre and millimetre radio maps show spatially resolved jet structures from sub-arcsecond to arcminute angular scales. They represent the most detailed investigation to date of the interaction of the relativistic jet from the X-ray binary with the young supernova remnant in which it is embedded. Comparison of projected jet axes at different wavelengths indicates significant rotation of the jet axis with increasing angular scale. This either suggests interactions of the jet material with surrounding media, creating bends in the jet flow path, or jet precession. We explore the latter hypothesis by successfully modelling the observed jet path using a kinematic jet model. If precession is the right interpretation and our modelling is correct, the best-fitting parameters describe an accreting source with mildly relativistic ejecta ($v = 0.5c$), inclined close to the plane of the sky ($i = 86^\circ$) and precessing over a 5-yr period.

Key words: accretion, accretion discs – stars: individual: Circinus X-1 – stars: neutron – ISM: jets and outflows – radio continuum: stars – X-rays: binaries.

1 INTRODUCTION

Neutron star X-ray binaries (NSXBs) present us with a key opportunity to study radio jet behaviour in the absence of a black hole engine, allowing them to act as a control sample with which to study the possible effects the presence of event horizons, ergospheres and other black hole related properties can have on jet formation (Migliari & Fender 2006). Unfortunately, neutron star jets are more difficult to study as the source group tends to be more radio quiet than their black hole counterparts, especially at lower X-ray luminosities (Fender & Kuulkers 2001; Migliari, Fender & van der Klis 2005; Gallo, Degenaar & van den Eijnden 2018), making their radio emission more challenging to detect. However, with recent advancement in radio telescope arrays and data reduction

techniques together with correct target selection, this can eventually be overcome.

Circinus X-1 (Cir X-1) is a confirmed NSXB (Linares et al. 2010) known for its regular 16.6 d flares (radio: Whelan et al. 1977, IR: Glass 1978, X-ray: Tennant, Fabian & Shafer 1986), believed to be the result of an eccentric orbit ($e \sim 0.40\text{--}45$) (Jonker, Nelemans & Bassa 2007; Johnston, Soria & Gibson 2016) and increased accretion at periastron. Attempts to further classify the system in terms of atoll and Z source behaviour are especially difficult based on its unique X-ray behaviour, with indicators reminiscent of atoll, Z source (Oosterbroek et al. 1995; Shirey et al. 1998) and even cases that fit neither during phases prior to periastron (Soleri et al. 2009b). Cir X-1 also displays relativistic jets, resolved at a variety of scales and wavelengths (X-ray: Heinz et al. 2007; Soleri et al. 2009a, radio: Stewart et al. 1993; Fender et al. 1998; Tudose et al. 2006). In the past, Cir X-1's flares were found to precede brightening of nearby ejecta, which was interpreted as

* E-mail: mickael.coriat@irap.omp.eu

re-energization via interaction with unseen outflows. The time delay between radio core flaring and re-brightening of the downstream material indicated very high Lorentz factors of $\Gamma > 15$ (Fender et al. 2004), and while the estimates have been corroborated via further advanced analysis of the same data sets (Tudose et al. 2008), subsequent observations of the source are yet to yield similar results (Calvelo et al. 2012a; Miller-Jones et al. 2012).

Cir X-1's quiescent and flare levels have varied significantly since discovery, with radio flares reaching >1 Jy in the late 1970s (Haynes et al. 1978; Nicolson, Glass & Feast 1980), but declining since ~ 1997 to reach only 10 s of mJy (Fender, Maccarone & van Kesteren 2005). Though interflare monitoring indicates the system remains historically 'faint', in the past few years Cir X-1 has begun to brighten in the radio band. Nicolson (2007) reported peak radio flares reaching Jansky-levels at 8.5 GHz for the first time in 20 yr, in observations with the HartRAO 26-m telescope. Following the return to strong X-ray flaring in 2010 June (Nakajima et al. 2010), Calvelo et al. (2010) reported flares >0.1 Jy. The last reported radio observing campaign on Cir X-1 carried out in 2012 with the Karoo Array Telescope test array KAT-7, revealed strong radio flaring at Jy-levels (Armstrong et al. 2013). Long-term X-ray monitoring of the system via the Monitor of All-sky X-ray Image (Matsuoka et al. 2009) campaign has shown that Cir X-1 remains in a faint state for the majority of time, but is punctuated by short periods (weeks to months) of intense activity when both periastron flares and interflare levels become far brighter than average.

A striking feature of Cir X-1's environment is the large-scale radio nebula in which the binary is embedded. Historically thought to be produced by the jets (Stewart et al. 1993), the nature of this nebula remained unclear until recent X-ray observations revealed an arcminute scale diffuse X-ray emission matching the structures observed in radio (Heinz et al. 2013). From morphological and spectral arguments, the nebula was identified as the remnant of the supernova that gave birth to the neutron star. The properties of the remnant, together with a refined distance of 9.4 kpc obtained with X-ray dust scattering light echoes (Heinz et al. 2015), placed an upper limit of $t < 5400$ yr on the age of the system. This upper limit makes Cir X-1 the youngest known X-ray binary and an important test case for the study of both neutron star formation and orbital evolution in X-ray binaries. The youthfulness of the system could explain its complex behaviour observed on short and long time-scales since the binary should still be settling down after the supernova explosion.

The orientation and morphology of the jets are among the complex features of the system. Over the years, Cir X-1's jets have been studied at various size scales from cm to mm wavelength observations leading to conflicting results. Calvelo et al. (2012a) reported on radio cm monitoring over a complete orbit of the binary and indicated that the system was behaving differently to what had been observed in the more active past. Lower levels of variability were found in structures around the system's core, the strongest of which were detected to the north-west: a region previously associated with the receding jet. Furthermore, the axis of near core resolved structure differs significantly from that previously observed, with the relatively similar intensity of the opposite components implying an inclination further from the line of sight. Calvelo et al. (2012b) reported on mm observations of Cir X-1, the first detection of a confirmed NSXB at mm wavelengths, and the subsequent image analysis provided evidence for sub-arcsecond jet structure around Cir X-1. This time, however, the structural axis indicated an angle closer to that of pre-2005 observations, albeit with the strongest signs of variability once again appearing to the north-west. Closer to the core, Miller-Jones et al. (2012) reported

on Australian Long Baseline Array (LBA) observations of Cir X-1 showing a near east–west jet axis on milli-arcsecond (mas) scales, as well as indications of a higher (almost perpendicular to the line of sight) jet inclination angle, visibly different from the cm and mm images of Calvelo et al. (2012a,b). Together, these results suggest that either Cir X-1's outflows have/are precessing or they have been deviated significantly from their former paths. Such a change could be recent, as the system showed little sign of precession over the previous decades of radio imaging (Tudose et al. 2008), though jet curvature has been visible on arcminute scales (20 cm; Tudose et al. 2006).

Unfortunately, the spacing between the above observations makes determining the origin of the variable jet axis difficult. Depending on outflow velocities and the rate of any precession that is present, one may generate a spectrum of possible variable helical structures. Alternatively, we may be dealing with a new quasi-static flow path resulting from jet kinks and interaction with media of variable density within the nebula. Further constraints on the origin can be applied if we observe the system at multiple frequencies within a short period of time, thus allowing us to probe the system on a range of scales while minimizing available time for structural variability to progress, and reveal any bends that may exist in the flows. This is the aim of the study presented in this paper. A description of the observations and the calibration process follows in Section 2. The radio maps obtained are analysed and discussed in Section 3 and concluding remarks are made in Section 4.

2 OBSERVATIONS & DATA PROCESSING

We conducted a set of centimetre and millimetre observations of Cir X-1 over three consecutive days on 2011 Dec 16, 17, and 18 during a quiescent radio phase preceding a radio flare that started on December 22 (Armstrong et al. 2013). We observed the source using the Australia Telescope Compact Array (ATCA) in 6A configuration (minimum baseline of 337m, maximum of 5939m) at 2.1 GHz (~ 14 cm), 5.5 GHz (~ 6 cm), 9.0 GHz (~ 3 cm), 33 and 35 GHz (~ 8.8 mm). The observing log is given in Table 1. Each frequency band was composed of 2048×1 -MHz channels (making the 33- and 35-GHz bands contiguous). For all our observations, we used PKS 1934-638 for absolute flux calibration. The sources used to calibrate the bandpass and the per-antenna complex gains as a function of time are listed in Table 1. Flagging and initial calibration were carried out with the Multichannel Image Reconstruction, Image Analysis, and Display (MIRIAD) software (Sault, Teuben & Wright 1995). In the sections next, we provide details on the additional data processing steps we applied on each data set. Note that independent of the tools and methods we employed, we used Briggs' weighting with a robust parameter of 0.5 to produce the images presented in this paper.

2.1 Millimetre data: 33 & 35 GHz

Since millimetre observations are more susceptible to atmospheric effects than those at longer wavelengths, phase stability had to be closely monitored via the ATCA 'seeing' monitor (output gives r.m.s. path length fluctuations in microns; see Middelberg, Sault & Kesteven 2006). These effects often increase as the runs progress, due to rising temperature and humidity. Upon analysis of the observations, it was found that large segments of data did not have sufficient phase stability to be reliable for imaging, making it necessary to define an adequate level of flagging that would improve final image fidelity. A maximum amount of de-correlation of 10 per cent arising from atmospheric seeing appears reasonable

Table 1. For each observation the table lists the date, observing frequency, start Modified Julian Day (MJD), total on-source time before and after flagging, orbital phase estimated from Nicolson (2007), r.m.s. noise level of the image, and measured flux density of the unresolved core component. We also indicate the bandpass and phase calibrators used. PKS 1934-638 was used for absolute flux calibration.

Date (UT)	Frequency (GHz)	MJD start	On-source time (h) [post-flag value (h)]	Orbital phase	r.m.s. ($\mu\text{Jy beam}^{-1}$)	S_{ν} (mJy)	Bandpass calibrator	Phase calibrator
2011 Dec 16	2.1	55910.75	9.67 [9.67]	0.67	50	12.80 ± 0.05	PKS 1934-638	PKS 1511-55
2011 Dec 17	33	55911.82	5.77 [3.66]	0.73	35	0.78 ± 0.04	PKS 1253-055	PKS 1511-55
2011 Dec 17	35	55911.82	5.77 [3.66]	0.73	35	0.68 ± 0.04	PKS 1253-055	PKS 1511-55
2011 Dec 18	5.5	55912.74	9.58 [9.58]	0.80	10	4.65 ± 0.01	PKS 1934-638	PKS 1520-58
2011 Dec 18	9.0	55912.74	9.58 [9.58]	0.80	12	3.11 ± 0.01	PKS 1934-638	PKS 1520-58

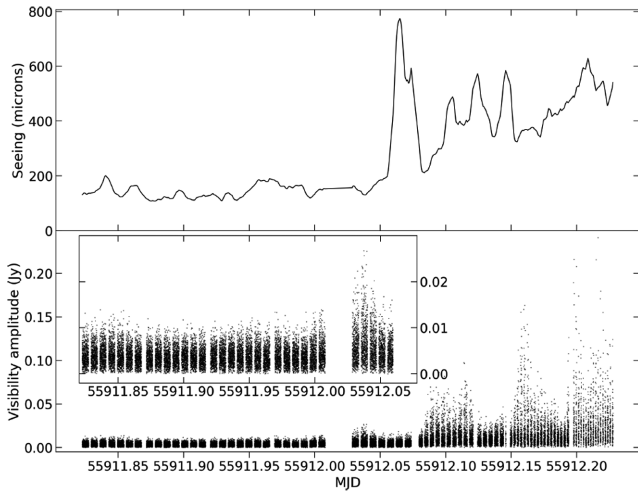


Figure 1. Cir X-1 seeing r.m.s. (top), and visibility amplitude (bottom) for the 2011 December 17 observation at mm wavelength (34 GHz). The inset in the bottom panel shows the data fraction that was used to produce images and the source measurements listed in Table 1.

for the purpose of our work. For the 10-min calibrator/target cycle time we used, the corresponding r.m.s. of the path length fluctuations for the ATCA in 6A configuration at a wavelength of 8.8 mm, is ~ 220 microns.¹ Segments whose majority of time was spent with r.m.s. higher than 220 microns were therefore excluded from subsequent analysis. Fig. 1 shows the visibility amplitudes and path length r.m.s. in microns for the mm observation on Dec 17. The second half of the observation suffered from poor phase stability and has been excluded. The time segment that we used to filter the 33- and 35-GHz data sets before imaging is shown in the inset of the bottom panel of Fig. 1. Post-flagging on-source time is also given in Table 1.

Once the individual 33 and 35 GHz complex gains were calibrated using external calibrator sources in MIRIAD, we converted the calibrated visibilities of the target field into measurement sets (MS) for further analysis with the Common Astronomy Software Application (CASA, McMullin et al. 2007). We applied a 32:1 frequency averaging to make the data volume more manageable.

¹Using equations (2) and (6) from Middelberg et al. (2006) with a baseline length of 6 km and a Kolmogorov exponent $\beta/2 = 0.33$. Note that during the second half of the observation, we decreased the target/calibrator cycle time down to 5, 3, and finally 2 min to minimize de-correlation. However, we could not reach less than 10 per cent de-correlation according to the calibrator cycle time calculator <https://www.narrabri.atnf.csiro.au/calibrators/calcycle.html>.

No time averaging was applied, so the standard 10 s integration time was preserved.

We produced the first images of the target field from the 33- and 35-GHz MS using straightforward multifrequency synthesis (MFS) de-convolution within the CLEAN algorithm in CASA. Cir X-1 is clearly detected at both frequency bands and is the only source visible in the field. The images revealed typical phase-error-related artefacts that we removed by performing three cycles of phase self-calibration using the CLEAN components map as sky model. A final amplitude and phase self-calibration cycle was performed to remove weak residual artefacts. We finally combined the 33- and 35-GHz self-calibrated visibilities into a single MS, which was imaged to form the final map shown in the left-hand panel of Fig. 2. We subtracted in the image plane a fitted point source at the location of Cir X-1's core to better reveal the jet components. The residual image is shown in the right-hand panel of Fig. 2.

2.2 Centimetre data: 5.5 and 9.0 GHz

We applied to the 5.5-GHz data set the same initial data reduction procedure as for the millimetre data. The first de-convolved images produced using MFS imaging showed significant radial artefacts affecting the central source Cir X-1. We performed a first standard phase self-calibration iteration with CASA; our sky model was the CLEAN component map obtained from a shallow de-convolution (100 CLEAN iterations). The strongest artefacts were removed, but some artefacts were still present and could not be suppressed by further iterations of self-calibration. These remaining artefacts corrupted the source spatial structure and geometry and therefore had to be removed for a proper analysis of the jets' properties. A possible origin of these stubborn artefacts could be intrinsic variability of the source during the observing time. Indeed, one of the main assumptions in aperture synthesis interferometry is that the sky brightness distribution is constant during the time of observation. If the variable source is the only (or the dominant) source in the field, its variability will be absorbed by the self-calibration gain-amplitude solutions. In the presence of other sources, variability over the synthesis time produces artefacts that cannot be removed by neither a standard de-convolution algorithm nor by self-calibration.

A calibration scheme that can solve for these effects must be employed and for these observations, the differential gains algorithm (Smirnov 2011) was used, implemented using the CALICO framework within the MEQTREES software package (Noordam & Smirnov 2010). The algorithm works by solving for additional complex gain terms against an assumed sky model for a selected subset of sources. The differential gains approach is intended to deal with the more general case of direction-dependent effects (DDEs), but readily adapts itself to the case of variable sources. Since

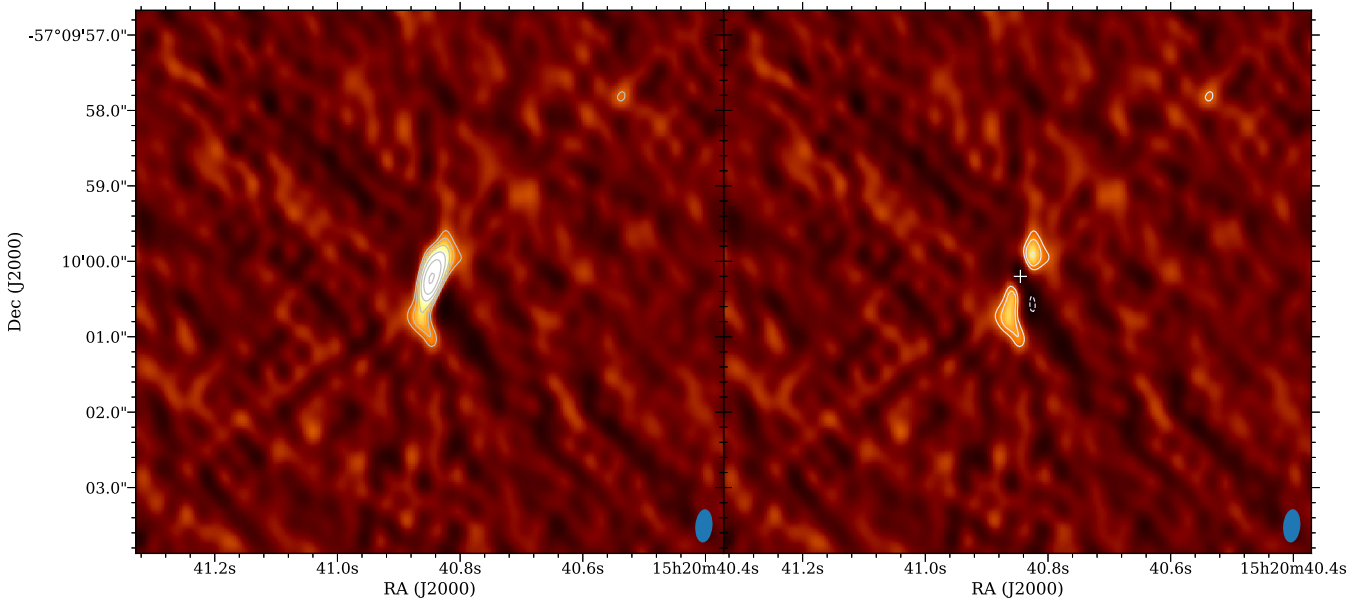


Figure 2. Cir X-1 ATCA radio images with overlaid contours of the combined 33 and 35 GHz (central wavelength of ~ 8.8 mm) MS. The left-hand panel shows the final map obtained after a self-calibration procedure (see text, Section 2.1). The right-hand map has had a fitted point source subtracted in the image plane at the location of the white cross, revealing symmetrical jet-like structures. The lowest contours correspond to $\pm 3\sigma$ (where $\sigma = 35 \mu\text{Jy beam}^{-1}$ is the r.m.s. noise level). Contours are then increased by $(\sqrt{2})^n \sigma$, where $n \in [1, 5]$. The synthesized beam size is $0.44 \times 0.23 \text{ arcsec}^2$ in position angle $-5^\circ.1$ and is shown at the bottom right-hand corner.

solving for direction-dependent gains increases the suppression of unmodelled sky sources (Nunhokee 2015), we must be careful to restrict the number of degrees of freedom (DoF) in the solution. A feature of the CALICO implementation allows one to constrain the differential gain term to be identical across all antennas, which makes it effectively a proxy for source variability, with the minimum number of DoFs. The measurement equation then becomes

$$\mathbf{V}_{pq} = \mathbf{G}_p(\Delta\mathbf{E}\mathbf{X}_0\Delta\mathbf{E}^H + \mathbf{X}_{\text{rest}})\mathbf{G}_q^H, \quad (1)$$

where \mathbf{V}_{pq} is the visibility matrix measured by the interferometer formed by antennas p and q , \mathbf{X}_0 are the model visibilities of the assumed variable source, and \mathbf{X}_{rest} are the model visibilities representing the rest of the local sky. H represents the Hermitian transpose. Both models need a non-negligible amount of flux for the global gains \mathbf{G}_p and the differential gains $\Delta\mathbf{E}$ to be independently constrained.

From the best image obtained with CASA, we created an initial sky model using PYBDSF (Mohan & Rafferty 2015) and TIGGER², where Cir X-1 was initially modelled by a single-point source and the rest of the sources in the field by Gaussian or point sources. We then self-calibrated the data against this sky model calculating \mathbf{G}_p as a function of time and frequency, using CALICO’s smooth gain solver mode (see Smirnov & Tasse 2015, for a description), which effectively corresponds to doing a weighted least-squares solution centred at each time/frequency point, with a Gaussian weighting kernel of 100 s and 640 MHz, respectively. We then computed the corrected residuals, i.e. the residual visibilities obtained after subtraction of the model and application of the gain corrections. Corrected residuals allow for a quick evaluation of the quality of the calibration. If the corrected residuals are noise-like then the combination of the sky model and gain corrections correctly represents the data. The first corrected residuals we obtained showed

symmetrical structures around the subtracted central point source as well as ring-like artefacts. We then attempted to account for variability, by solving for $\Delta\mathbf{E}$ with a Gaussian weighting kernel of 15 min (and no variation in frequency), and we kept the same time/frequency smoothing kernels as before for the \mathbf{G}_p solution. The corrected residuals we obtain after one calibration cycle were improved, but the symmetrical structures were still present together with a negative hole at the location of the subtracted point source. This indicated that a single variable point source was not a good representation of the data. Therefore, we added two-point sources to the sky model at the locations of the residual structures to account for the potential presence of jets. We first calibrated against this new sky model without the differential gain term and allowing the positions of the two-point sources to vary from one calibration cycle to another. The symmetrical structures were finally removed but the residuals at the location of the central source were still unsatisfactory. We then added back the differential gain term for the central point source and performed another cycle of self-calibration/imaging, which finally yielded noise-like residuals. Fig. 3 shows the final image (where we can distinguish the nebula surrounding Cir X-1) together with a close-up view of the central region where the core component has been subtracted to emphasize the jets.

The 5.5- and 9.0-GHz data were obtained simultaneously because of the dual-frequency observation capabilities of the ATCA. Unsurprisingly, the 9.0-GHz images suffered from the same kind of corruption as the 5.5-GHz data. We thus employed the same calibration strategy and obtained the radio maps presented in Fig. 4.

2.3 Centimetre data: 2.1 GHz

As we move to lower observing frequencies, the field of emitting sources surrounding Cir X-1 becomes increasingly complex. At 2.1 GHz, this field contains various type of sources ranging from

²<https://github.com/ska-sa/tigger>

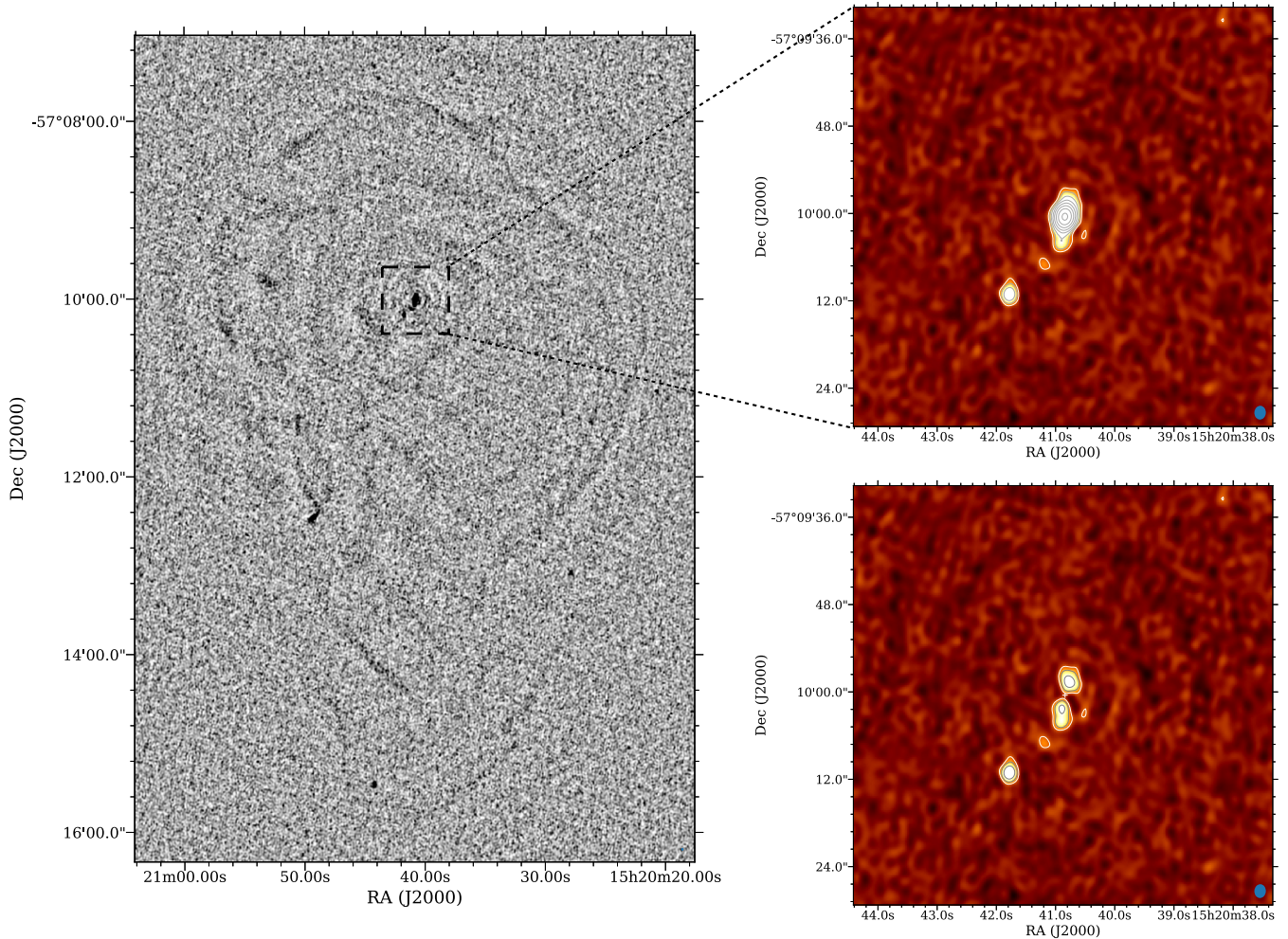


Figure 3. Cir X-1 ATCA radio images at 5.5 GHz. The left-hand panel shows the full size map obtained after self-calibration with MEQTREES using the differential gains algorithm to absorb intrinsic variability. We can see Cir X-1 at the centre surrounded by its nebula. High-contrast grey scale has been chosen here to accentuate the (otherwise weak) structures of the nebula. The top right-hand panel is a close-up view of the central region showing Cir X-1 and a weak source at the south-east, which is presumably a background source. The bottom right-hand panel shows the same close-up where the central variable source has been subtracted to unveil the jets. The white cross indicates the location of the subtracted source. The contour levels in the right-hand panel maps begin at 3σ (where $\sigma = 10 \mu\text{Jy beam}^{-1}$ is the r.m.s. noise level) and increase in multiples of 2. A single, dashed negative contour is included with a value of -3σ . The synthesized beam size is $1.9 \times 1.6 \text{ arcsec}^2$ in position angle $-3^\circ.7$ and is shown at the bottom right-hand corner.

strong and compact to faint and extended (e.g. Cir X-1’s nebula) including partially extended, moderately bright, morphologically complex sources (to which Cir X-1 belongs). Preliminary images also revealed the need of imaging well outside the primary beam FWHM (~ 30 arcmin) due to the presence of strong peripheral sources producing sidelobes encroaching into the central part of the image. De-convolution and imaging of such a field then becomes a challenge as DDEs come into play adding to the intrinsic complexity of the source population. The best image we could obtain using standard imaging methods and direction independent self-calibration is presented in the top panel of Fig. 5. Numerous circular and radial artefacts are visible. This makes the field truly DDE limited (unlike the 5.5- and 9.0-GHz case, where only intrinsic source variability was of concern). We therefore took a different approach to the calibration, employing the new KILLMS³ calibration

package combined with the DDFACET⁴ imager (Tasse et al. 2018). We provide below a brief description of these new software packages.

The new generation of radio interferometers (SKA precursors and pathfinders as well as the upgrades of the current radio observatories) are characterized by wide fields of view, large fractional bandwidth, high sensitivity, and high resolution. These superior performances introduce new issues for calibration and imaging due to complex signal corrupting effects that were negligible with the older generation of instruments. These effects can be of instrumental (e.g. pointing errors, dish deformation, antenna coupling within phased arrays) or astrophysical origin (e.g. the ionosphere and its associated Faraday rotation) and are often characterized by the levels of corruption varying across the field of view (being as well baseline, time, and frequency dependent). Correcting these direction-dependent effects is a complex and com-

³<https://github.com/saopicc/killms>

⁴<https://github.com/saopicc/DDFacet>

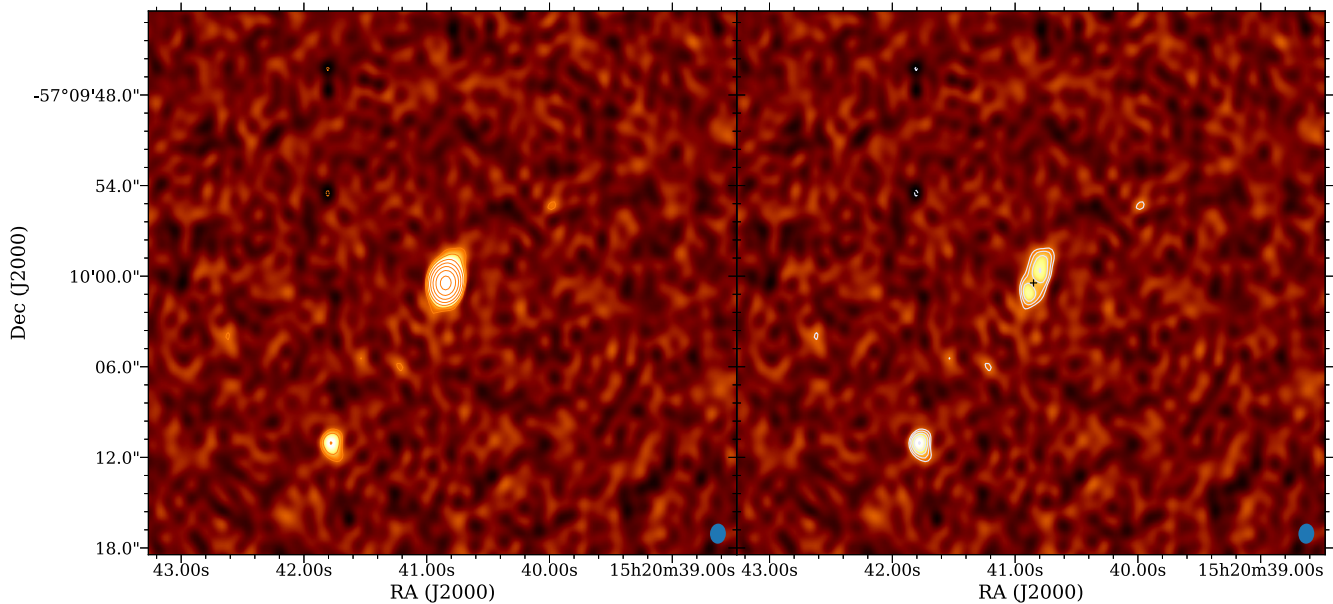


Figure 4. Cir X-1 ATCA radio images at 9.0 GHz. The left-hand panel shows the map obtained after self-calibration with MEQTREES using the differential gains algorithm to absorb intrinsic variability. The weak (presumably background) source visible in the 5.5-GHz map to the south-east of Cir X-1 is also detected in this map. The right-hand panel shows the image where the central variable source has been subtracted to reveal the jets. The black cross indicates the location of the subtracted source. The lowest contours correspond to $\pm 3\sigma$ (where $\sigma = 12 \mu\text{Jy beam}^{-1}$ is the r.m.s. noise level). Contours are then increased by $(\sqrt{2})^n \sigma$, where $n \in [1, 5]$ for the right-hand panel and only in multiples of 2 for the left-hand panel for clarity. The synthesized beam size is 1.3×1.1 arcsec² in position angle $-3^\circ.8$ and is shown at the bottom right-hand corner.

putationally expensive process as it consists in inverting a very large and often ill-conditioned system of non-linear equations. KILLMS implements two very efficient algorithms for solving this direction-dependent calibration problem. The COHJONES and KAFCA solvers use optimization techniques based on the properties of the complex (‘Wirtinger’) Jacobian. The mathematical framework and related algorithmic implementation are described in Tasse (2014) and Smirnov & Tasse (2015), respectively.

DDFACET is a wide-band wide-field imager based on a coplanar faceting scheme (Tasse et al. 2018). It implements new deconvolution algorithms and can account for externally defined gain corrections and beam patterns. It was designed to work in concert with KILLMS. In each of the defined direction (i.e. region; see an example in Fig. 5 top panel), a different set of Jones matrices is taken into account by DDFACET during the deconvolution cycle. Here, since the ATCA primary beam at 2.1 GHz is poorly constrained beyond the first minimum,⁵ we simply work with apparent flux densities and the Jones matrices being considered are the calibration solutions produced by KILLMS (one scalar solution per direction, antenna, time, and frequency).

To obtain the final image presented in the bottom panel of Fig. 5, we applied the following calibration and imaging procedure: We first produced an image with DDFACET using direction-independent faceting and the wide-band hybrid matching pursuit (HMP) deconvolution algorithm.⁶ From this preliminary image, we made a sky model and clustered the sky in seven directions corresponding to the directions of the seven brightest sources in the field. This

decomposition in seven regions is illustrated by the polygons shown in the top panel of Fig. 5. We also created a deconvolution mask using a threshold-based algorithm combined with manual inclusions/exclusions of specific regions of the sky, e.g. excluding strong artefacts and including faint and extended sources. From the sky model and the cluster nodes catalogue, we computed antenna–time–frequency–direction dependent gain corrections using the COHJONES algorithm within KILLMS. For this first pass, we used time and frequency solution intervals of 10 min and 256 MHz, respectively. The obtained calibration solutions were applied during the subsequent deconvolution and imaging step with DDFACET. With the created mask, we then used the sub-space deconvolution algorithm in DDFACET instead of HMP as it improves deconvolution of extended emission. We repeated this calibration/imaging cycle twice, improving sky model and mask at each round and reducing the frequency solution interval down to 64 MHz (we kept the same time bin of 10 min as lower values provided poorer results). Most of the artefacts have disappeared in the final image shown in the bottom panel of Fig. 5. Some weak residual structures remain at the noise level around a few sources, but they do not affect the central region, where Cir X-1 is located.

If Cir X-1 was variable during the course of the 2.1-GHz observation, the facet containing it should have shown similar issues as the 5.5- and 9.0-GHz images. Yet, a single gain solution for the entire facet was enough to remove the artefacts, which indicate that the source was likely not (or weakly) variable. This is consistent with the time sequence of our observations. We first observed at 2.1 GHz on December 16 (orbital phase 0.67), then at 33 and 35 GHz on December 17 (orbital phase 0.73), and finally at 5.5 and 9.0 GHz on December 18 (orbital phase 0.80). The later observation was the closest in time to the radio flare detected on December 22 that might explain why it is the only observation where variability was significant.

⁵see http://www.narrabri.atnf.csiro.au/people/ste616/beamshapes/beamshape_16cm.html

⁶An improved analogue of the multiscale multifrequency CLEAN algorithm. See Tasse et al. (2018) for details.

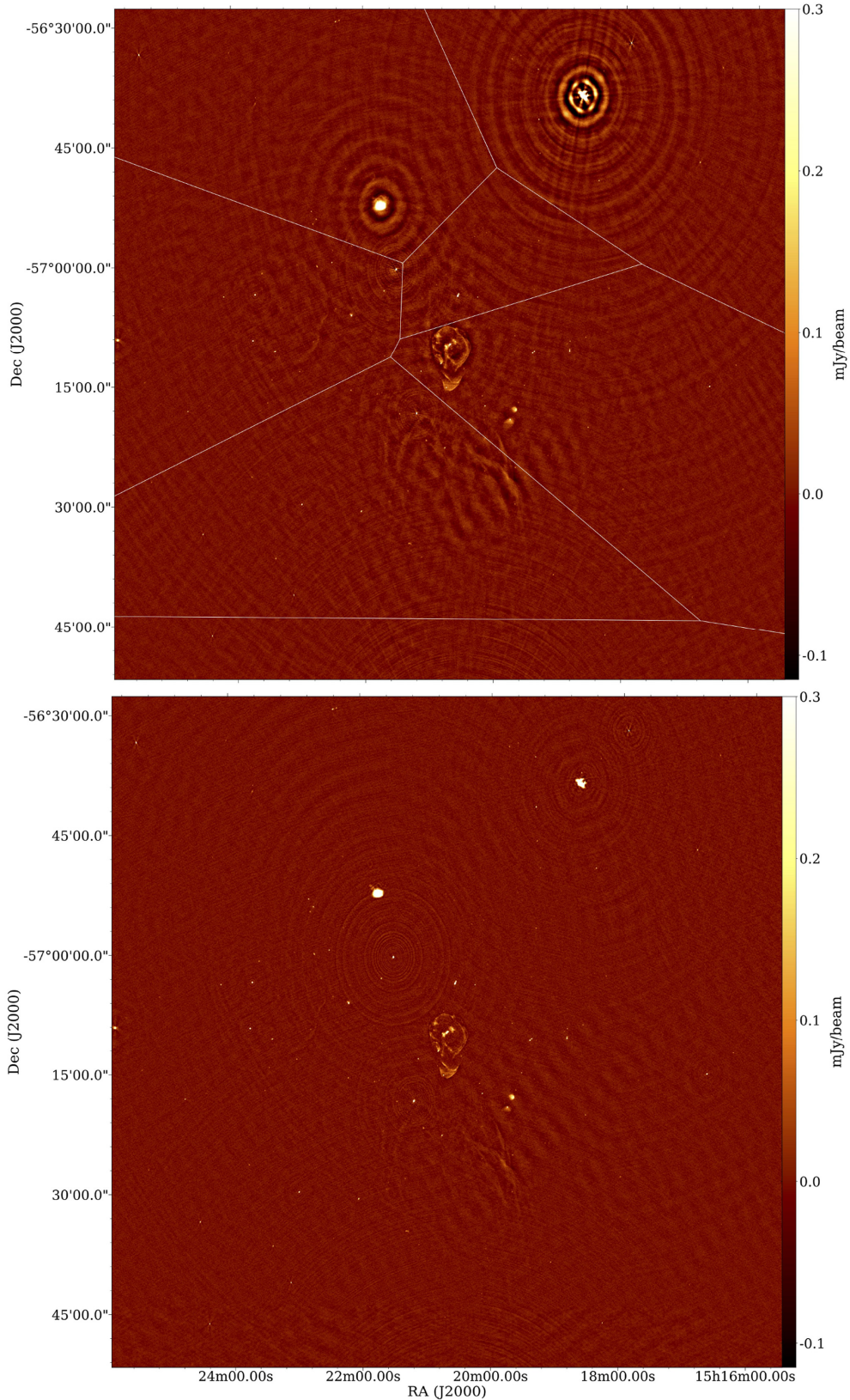


Figure 5. ATCA large-scale radio images at 2.1 GHz of Cir X-1’s field. Top panel: Best image obtained after standard self-calibration and imaging. The colour bar shows the radio brightness in units of mJy beam^{-1} . Bottom panel: Image obtained after direction-dependent calibration and imaging using KILLMS and DDFACET. The polygons overlaid on the top panel correspond to the seven regions for which independent calibration solutions have been computed (see Section 2.3). The southern-most region is only partially displayed as we only show the central two-third of the full-size image. Cir X-1 and its nebula are located at the centre of the image. The field contains a set moderately strong and morphologically complex sources within and beyond the primary beam FWHM (~ 30 arcmin) as well as faint and extended structures.

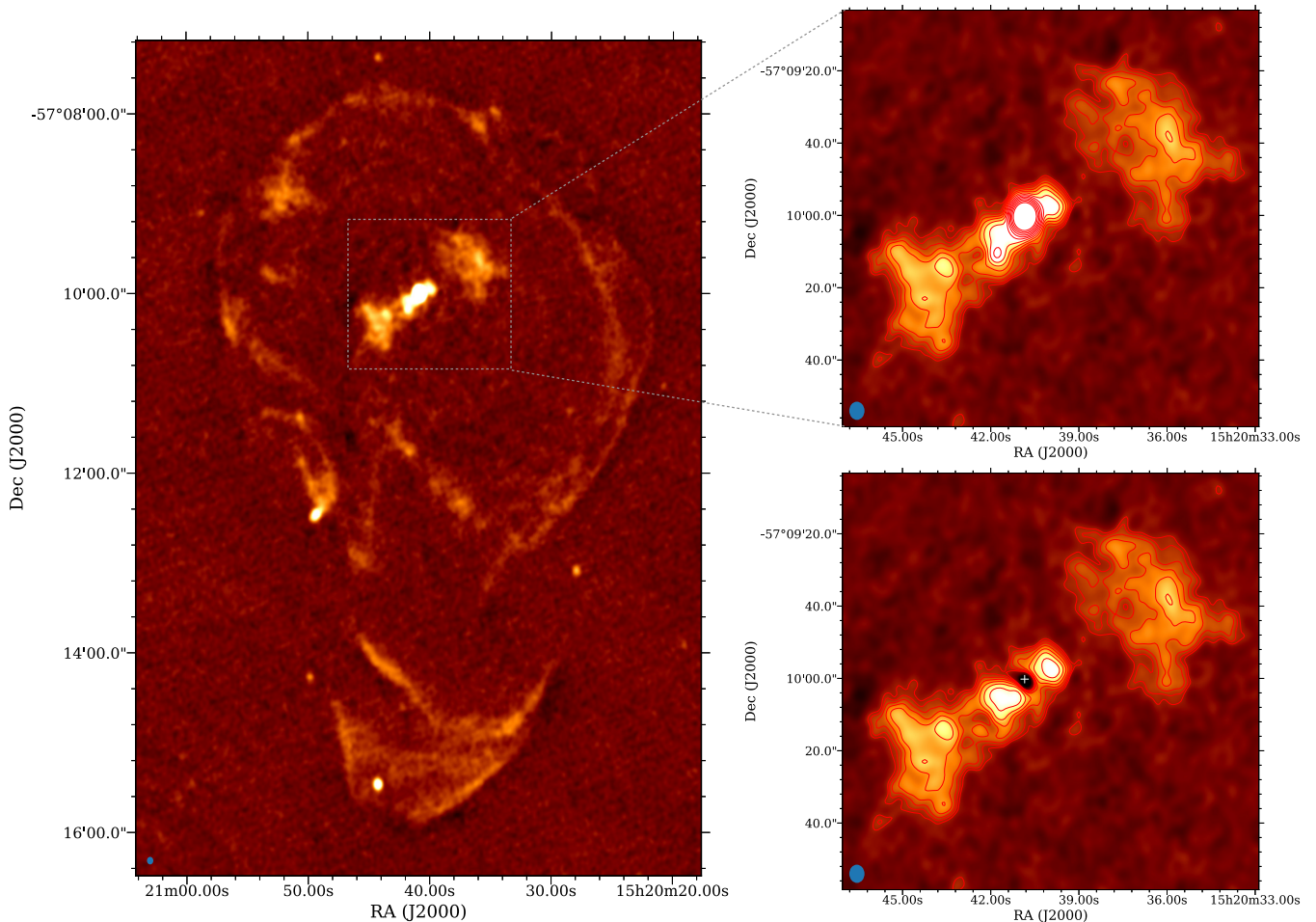


Figure 6. Cir X-1 ATCA radio images at 2.1 GHz. The left-hand panel shows the supernova remnant surrounding Cir X-1. The top right-hand panel is a close-up view of the central region, where we clearly detect Cir X-1 together with extended jet structures. The two lobes to the SE and NW (also detected in X-rays) are likely due to the interaction of the jets with surrounding media within the nebula. Contours are overlaid and start at $\pm 3\sigma$ (where $\sigma = 14 \mu\text{Jy beam}^{-1}$ is the r.m.s. noise level) and increase by $(\sqrt{2})^n \sigma$, where $n \in [1, 7]$. The background source to the SE detected in the 5.5- and 9.0-GHz images is also visible, although it is partially blended with the surrounding jet emission. The bottom right-hand panel shows the same image where we have subtracted, in the image plane, the core source (location marked by the white cross) as well as the SE background source for clarity. The synthesized beam size is 5.0×4.2 arcsec² in position angle $1^\circ.4$ and is shown at the bottom left-hand corner.

Fig. 6 (left-hand panel) shows a close-up view of this central region where the remnant surrounding Cir X-1 is now clearly visible. Zoomed-in views of Cir X-1 itself and its jets are shown in the right-hand panels of Fig. 6. As for the data sets at higher frequencies, we subtracted the contribution of the unresolved core radio emission to focus on the double-sided jets structure. Note that the scale of these structures are the largest on which we can be confident that the jets dominate over the remnant in terms of morphology.

3 RESULTS & DISCUSSION

3.1 Jet flux and morphology

After subtraction of the core emission as described in the previous section, we measured the flux density and position of the jet components for each frequency band by fitting point sources to the image plane. The majority of the jet components being unresolved, only a single-point source per component was necessary. However, the southern components of the 5- and 2.1-GHz jets are both slightly resolved. Two-point sources were required to model each one of

them. The top and middle panels of Fig. 7 show the jets flux density as well as the south to north jet flux ratio as a function of projected distance from the core,⁷ where we used the coordinates of the 34-GHz core source as reference. The southern jet components of the 5.5 and 2.1 GHz being modelled by two-point sources each, while their corresponding northern components comprise a single-point source only, we calculated two flux ratios for each data set and plotted them against the distance of the southern components

From this figure we note that, on average, the northern jet is slightly brighter than its southern counterpart albeit the flux ratio does not exceed two. This first excludes the possibility of a highly relativistic jet seen at low inclination with respect to the line of sight. It also suggests that the northern jet is the approaching one. In the bottom panel of Fig. 7, we plot the jet axis position angle as a function of distance to the core. For comparison, we also include the jet position angle measured at milliarcsecond scale with the

⁷We do not present the flux densities in the form of a spectrum as the jet components are not spatially coincident.

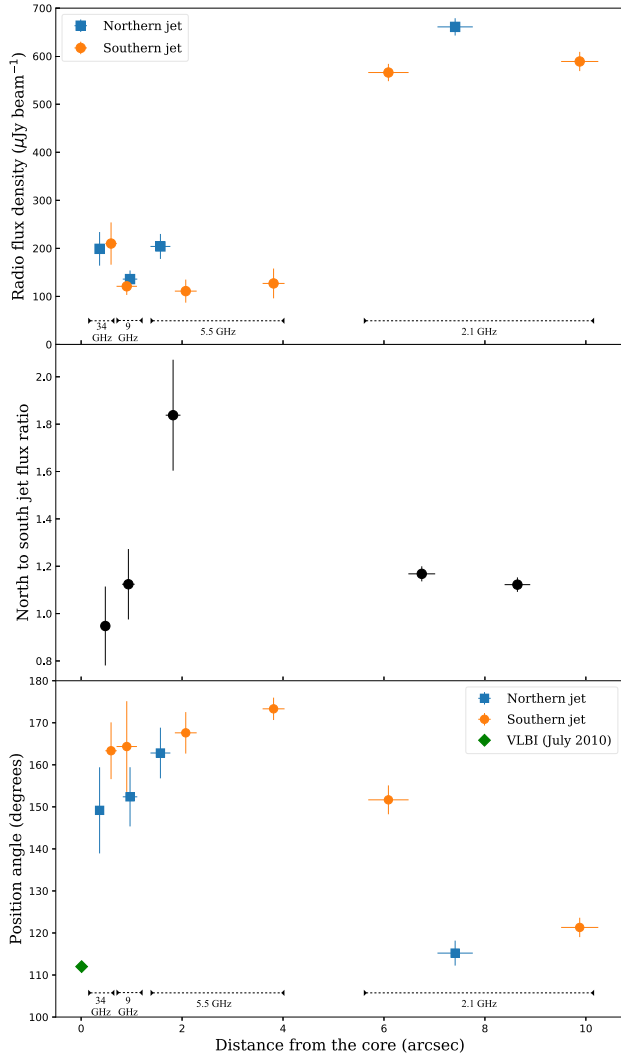


Figure 7. Radio flux densities (top panel), north to south jet flux ratio (middle panel), and jet position angle (bottom panel) as a function of distance to the core. Position and fluxes were obtained by fitting point sources to the northern and southern jet components in the image plane. Error on the positions are estimated as the PSF size divided by twice the local signal-to-noise ratio (see e.g. Fomalont 1999). The bottom panel also includes the position angle of the jet measured at milliarcsecond scale in 2010 July by Miller-Jones et al. (2012). Note that the jet flux ratios are plotted against the mean distance of each component pairs.

LBA in 2010 July (17 months before our observations) by Miller-Jones et al. (2012). A more qualitative view of the jet morphology is presented in Fig. 8, where we overlay the jet contours at 5.5, 9.0, and 34 GHz on the 2.1-GHz image. Both figures indicate significant variations of the jets orientation with increasing distance from the core. This flow path could obviously result from jet kinks and/or interactions with media of variable density within the nebula. Alternatively, a precessing jet may also produce a similar pattern. The later interpretation would also naturally explain the fact that the positions of the jet components change symmetrically with respect to the centre when moving away from the core. In addition, we note from Fig. 7 that the jet axis does not vary monotonically. Its position angle first increases then decreases with increasing distance from the core, suggesting a form of oscillation. Finally, the angular extent of the radio lobes located at ~ 40 arcsec from the core (see

Fig. 8; Sell et al. 2010; Heinz et al. 2013, for the X-ray counterpart) also suggests precession if we assume the lobes originate from interaction of the jets with the nebula. We thus explore further this scenario in the section next.

3.2 Jet precession modelling

In order to evaluate if a precessing jet could reproduce our data, we adapted the kinematic jet model of Hjellming & Johnston (1981) initially developed to explain the jet morphology of the well-known microquasar SS433. The details of the model can be found in the aforementioned article. We recall next the main parameters:

i : inclination of the jet precession axis with respect to the line of sight.

ψ : half-opening angle of the jet precession cone.

χ : position angle of the jet precession axis in the plane of the sky (positive from north to east).

P : precession period.

v : jet velocity. The model assumes constant velocity.

d : distance to the source.

ϕ_{prec} : precession phase.

s_{jet} : jet sign parameter. +1 for the approaching jet, -1 for the receding jet.

s_{rot} : sense of rotation. +1 corresponds to counterclockwise, -1 to clockwise.

For a given time t_0 , the model computes the position of a particular twin jet pair ejected at time t_{ej} , in the form of right ascension and declination offsets from the core position, $\Delta\alpha_{\text{mod}}$ and $\Delta\delta_{\text{mod}}$, respectively. Considering all the possible values of $t_{\text{ej}} < t_0$, we obtain a snapshot of the model jet at time t_0 , projected on the plane of the sky. The fitting procedure then requires an objective function to be minimized and that describes the quality of the fit. We require that a good solution be one that minimizes the sum of the minimum distances of the data points to the model in the $(\Delta\alpha, \Delta\delta)$ plane. Ideally, any data point would sit on the model curve and the minimal distances would be zero for a perfect solution. Thus, we define our objective function as follows:

$$S = \Upsilon(\beta, i) + \sum_i \left[\frac{(\Delta\alpha_i - \Delta\alpha_{\text{mod}_i})^2}{\sigma_{\alpha_i}^2} + \frac{(\Delta\delta_i - \Delta\delta_{\text{mod}_i})^2}{\sigma_{\delta_i}^2} \right], \quad (2)$$

where $\Delta\alpha_i$ and $\Delta\delta_i$ are, respectively, the right ascension and declination offset of the i th data point with associated errors σ_{α_i} and σ_{δ_i} . The chosen model $(\Delta\alpha_{\text{mod}_i}, \Delta\delta_{\text{mod}_i})$ pair is the one that minimizes the square distance between the precession helix and the observed $(\Delta\alpha_i, \Delta\delta_i)$ pair. To guarantee that our jet-precession modelling will also predict velocities and inclinations in agreement with the observed jet flux ratio, we included a penalty function $\Upsilon(\beta, i)$ based on the analytical expression of the approaching to receding jet flux ratio $\frac{F_{\text{app}}}{F_{\text{rec}}}$:

$$\Upsilon(\beta, i) = \begin{cases} 0, & \text{if } 0.8 < \frac{F_{\text{app}}}{F_{\text{rec}}} = \left(\frac{1+\beta \cos i}{1-\beta \cos i} \right)^n < 2, \\ 100, & \text{elsewhere,} \end{cases} \quad (3)$$

where $\beta = \frac{v}{c}$ is the velocity (in units of the speed of light) and n depends on the geometry and spectral index of the jet and is typically in the range between two and four (we have used an intermediate value of three). The choice of a penalty $\Upsilon(\beta, i) = 100$ effectively guarantees that any tentative solution providing $\frac{F_{\text{app}}}{F_{\text{rec}}} > 2$ or < 0.8 (values based on the measured flux ratios, see Fig. 7) is statistically disfavoured during optimization. Here, we simply set bounds to the jet flux ratios as we do for the other parameters (see next).

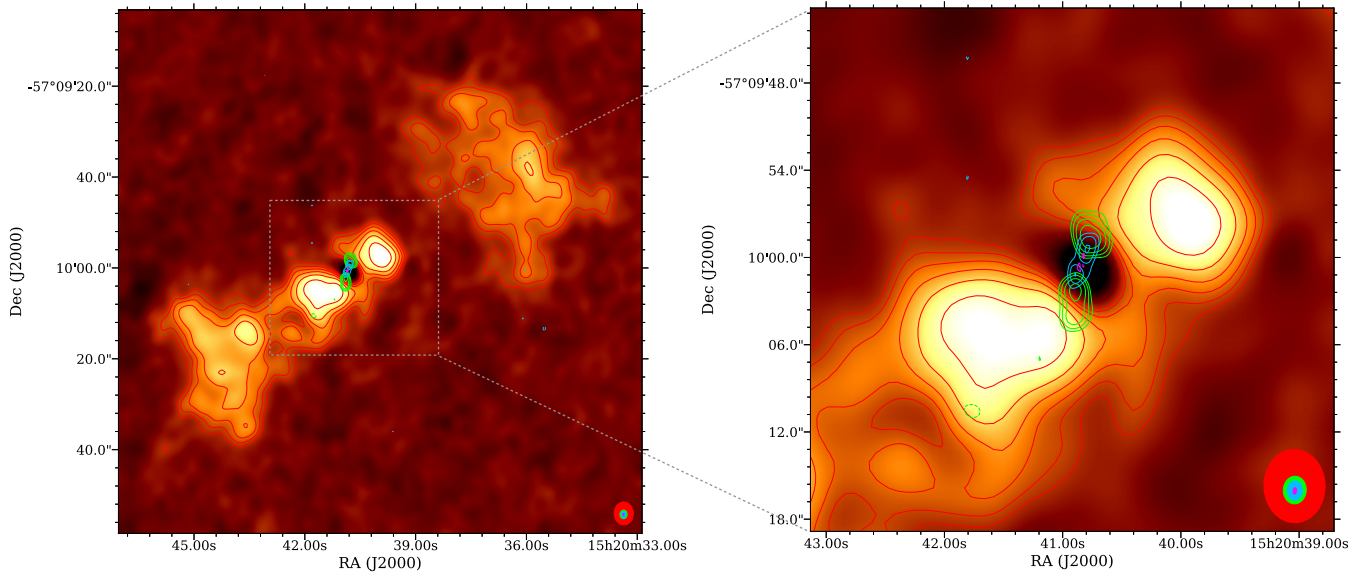


Figure 8. Central region of the 2.1-GHz image of Cir X-1 with overlaid contours (listed in order of decreasing distance to the core) at 2.1 GHz (red), 5.5 GHz (green), 9.0 GHz (blue), and 34 GHz (magenta). For each frequency band, the central core source has been removed to focus on the jet morphology. The contour levels are the same as those presented in Fig. 2, Fig. 3, Figs 4, and 6. The synthesized beams corresponding to each observing frequency are shown at the bottom right-hand corner of the images with the same colour code as the one used for the contours and with size decreasing with increasing frequency.

Regarding the optimization process itself, preliminary tests using standard gradient-based algorithms indicated that the objective function had many local minima in which the algorithm easily got trapped. We therefore adopted a global optimization approach more suited to our problem. We used the ‘differential evolution’ algorithm (Storn & Price 1997) implemented in the SCIPY.OPTIMIZE package. The algorithm requires bounds for each parameter; we therefore defined the parameter space as follows:

i : from 0° to 90°

ψ : we constrained the half-opening angle of the jet precession cone to remain in the range 20 – 50° in order to match the half-opening angle of 35° of the extended lobe structures that we assume result from interactions of the jets with the nebula (see e.g. Sell et al. 2010).

χ : similarly, the position angle of the jet precession axis is restricted to the 110 – 140° range to match the position angle of the lobes.

v : from 10^{-2} to $0.99c$

P : from 10 to 3000 d. Preliminary tests have shown that outside these boundaries (and for the velocity range adopted above) the model tends to either a straight line ($P > 3000$ d) or a helix that entirely fills the space.

d : we fixed the distance to 9.4 kpc based on Heinz et al. (2015).

ϕ_{prec} : from 0 to 2π

s_{jet} : fixed to -1 for the southern jet (receding) and $+1$ for the northern jet (approaching).

s_{rot} : fixed for a given optimization run. Both $+1$ (counterclockwise) and -1 (clockwise) were tested.

We obtain the best fit with the parameters listed in Table 2. The associated uncertainties have been obtained using a Monte Carlo Markov Chain (MCMC) analysis and correspond to a 1σ quantile, estimated as half the difference between the 15.8 and 84.2 percentiles. Note that we fixed the distance to 9.4 kpc, while Heinz et al. (2015) provide an error range of $9.4^{+0.8}_{-1.0}$ kpc. These uncertainties will primarily impact the estimated jet velocity. To

Table 2. Best-fitting parameters of the precessing jet model applied to Cir X-1’s radio jets.

Parameter	Best-fitting value
Half-opening angle of the precession cone	$\psi = 31 \pm 5^\circ$
Inclination of the jet precession axis with respect to the l.o.s.	$i = 86 \pm 7^\circ$
Position angle of the jet precession axis	$\chi = 134 \pm 6^\circ$
Precession period	$P = 1821 \pm 503$ d
Precession phase ^a	$\phi_{\text{prec}} = 1.1\pi \pm 0.3$
Jet velocity	$v_{\text{jet}} = (0.5 \pm 0.2)c$
Distance	$d = 9.4$ kpc (fixed)
Approaching jet (N)	$s_{\text{jet}} = +1$ (fixed)
Receding jet (S)	$s_{\text{jet}} = -1$ (fixed)
Sense of rotation (counterclockwise)	$s_{\text{rot}} = +1$

^aIn fitting the model to the data, we implicitly assumed that the variation of the precession phase was negligible over the 3 d of observation, which is consistent with the 1821-d precession period obtained. Therefore, the precession phase provided here corresponds to an average over our observing days.

measure this impact, we ran an MCMC analysis fixing all the parameters to their best-fitting value except velocity and distance, the latter being free to vary between 8.4 and 10.2 kpc. We derive a 1σ error of $0.06c$ on the velocity due to the uncertainty on the distance. The error bar on the velocity provided in Table 2 takes into account this additional source of uncertainty.

Data points and jet model are plotted in Fig. 9, while Fig. 10 shows the model overlaid on the radio contours and image. The model depicts a source with mildly relativistic jets ($v \sim 0.5c$), inclined close to the plane of the sky ($i \sim 86^\circ$) and precessing over a period of approximately 5 yr. Despite being simple, as it assumes continuous ejection at constant velocity (which is likely not the case), the model successfully reproduces the jet flow path. This is obviously not a proof that precession is the correct interpretation nor that the set of parameters we find is unique. This essentially demonstrates that precession is a valid interpretation. As a consistency check, using

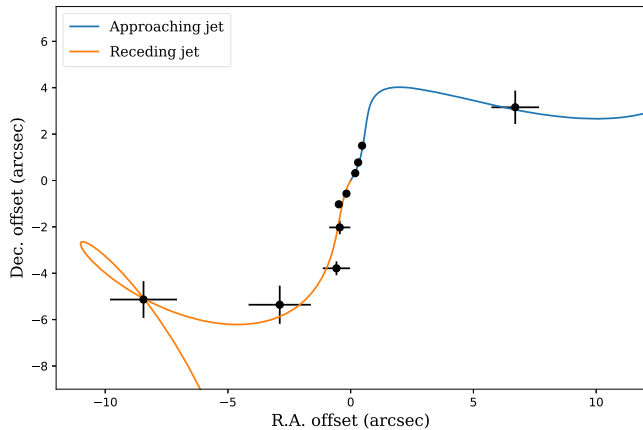


Figure 9. Positions of the jet components, plotted as RA and Dec. offsets from the core, together with the best-fitting precessing jet model whose parameters are given in Table 2. The approaching jet (North-West) is represented in blue and the receding jet (South-East) in orange. Note that ‘approaching’ and ‘receding’ refer here to the orientation of the jet precession axis w.r.t. the line of sight. However, this axis is oriented at 86° to the line of sight and given the half-opening angle of 31° of the precession cone, each jet component will switch from approaching to receding, and vice-versa, every precession cycle.

our best-fitting parameters, we calculated the jet position angle and the north-to-south jet flux ratio predicted by the model if we were observing at mas scale on 2010 July 28 (507 d before our observations), the date of the LBA observations of Miller-Jones et al. (2012). At a distance of 10 mas from the core, the model predicts a position angle of $105 \pm 8^\circ$ and a jet flux ratio of 0.60 ± 0.26 , which is in global agreement with the position angle of $112 \pm 1.5^\circ$ and the jet flux ratio of 0.71 ± 0.11 measured⁸ by Miller-Jones et al.

Finally, it is interesting to note that Cir X-1 has been recently proven to be the youngest known X-ray binary by constraining the age of its surrounding supernova remnant (Heinz et al. 2013). The only other established Galactic X-ray binary with a supernova remnant is the black hole candidate SS433 (Geldzahler, Pauls & Salter 1980). Indications that jets could also be precessing in Cir X-1 add further similarities between the two sources. It suggests that precession is related to the young age of these systems where alignment of the spin of the two components with the orbital axis has not been achieved yet. Furthermore, the mass transfer may not have started immediately after the supernova, further reducing the time available for spin-orbit alignment. (see e.g. Brandt & Podsiadlowski 1995; Martin, Tout & Pringle 2008 and discussion in Heinz et al. 2013).

3.3 Precession period

The precession period we obtain seems particularly long when compared with precession periods observed in black hole X-ray binaries that are typically of the order of tens to few hundred days (e.g. 162.5 d for SS433, Eikenberry et al. 2001, or 485 d for 1E 1740.7–2942, Luque-Escamilla, Martí & Martínez-Aroza 2015). To our knowledge, there is no reported jet precession period for an

⁸There is no uncertainty reported on the jet position angle in Miller-Jones et al. (2012). We estimated an error of 1.5° on the jet angle based on the reported PSF size and SNR. The jet flux ratio and associated error has been estimated from the contours and the rms noise level of their fig. 2b.

(confirmed) NSXB we could straightforwardly compare our results with. The nature of the compact object could be the origin of this notable difference in precession periods between Cir X-1 and the black hole X-ray binaries. We note, however, that Rajoelimanana, Charles & Udalski (2011) reported superorbital periodicities in Be X-ray binaries in the Small Magellanic Cloud, some of which were greater than 1000 d, for orbital periods of a few tens of days. The authors attribute these long-term variability to properties of the Be star disc, though. While the nature of the companion star is still unclear in Cir X-1, the possibility of a Be star is not favoured due to the lack of double-peaked lines in optical and infrared spectra and an orbital period shorter than any other Be/X-ray binaries (see discussion in Johnston et al. 2016).

From the current literature, it is not obvious that a 5-yr precession period could be explained by the theory of an underlying warped accretion disc driving the precession of the jets. Although it is beyond the scope of this paper to investigate this aspect in detail, some simple estimates can be made. As an example, Massi & Zimmermann (2010) examine two mechanisms, tidal and Lense–Thirring precessions, to explain the precession of the jets in the gamma-ray binary LS I +61°303, a compact object on an eccentric orbit around a Be-type star (Taylor & Gregory 1982; Casares et al. 2005). As stated in Massi & Zimmermann, precession of an accretion disc could result from the misalignment of the compact object rotational axis with respect to the orbital plane; a misalignment produced by an asymmetric supernova explosion of the progenitor. Then, two resulting configurations can be considered: either the disc is mostly coplanar with the rotational plane of the compact object and would therefore be subject to the gravitational torque of the companion star, or the disc is mostly coplanar with the orbital plane and tilted w.r.t. the compact object, which would induce Lense–Thirring precession. The latter mechanism can be excluded in our case as it produces only precession periods shorter than a few days for a large range of parameters (see Massi & Zimmermann 2010). On the other hand, tidal precession leads to precession periods of a few hundred days or longer, which is more consistent with our results. We can thus try and put constraints on the system configuration assuming tidal precession is the driving mechanism. Following Larwood (1998), we can write the accretion disc outer radius as a fraction β of the Roche lobe radius. Then, combining equation (4) from Larwood (1998) with the analytical expression of the Roche radius given by Eggleton (1983), we can write the expected precession period as follows:

$$P_{\text{tidal}} = \frac{7}{3} \frac{P_{\text{orb}}}{\cos \delta} \frac{(1 + \mu)^{1/2}}{\mu} \left(\frac{0.49\beta}{0.6 + \mu^{2/3} \ln(1 + \mu^{-1/3})} \right)^{-3/2}, \quad (4)$$

where P_{orb} is the orbital period, δ is the inclination angle of the accretion disc with respect to the orbit, and $\mu = \frac{M_s}{M_{\text{neutron star}}}$ is the mass ratio. As mentioned earlier, the nature of the companion star is uncertain. Possibilities range from a low-mass companion (Johnston et al. 2016) to a B5 supergiant (Jonker et al. 2007). Taking $M_{\text{neutron star}} = 1.4 M_\odot$, we must therefore consider the range 0.1–4.2 for the mass ratio. In addition, assuming the jet precession axis is orthogonal to the accretion disc plane implies $\delta = \psi = 31^\circ$, the half-opening angle of the precession cone in our model. Using these parameters together with $P_{\text{orb}} = 16.6$ d and $P_{\text{tidal}} = 1821$ d, we plot in Fig. 11 β as a function μ . The figure shows that a 5-yr precession period can be achieved for β values between 0.2 and 0.7 depending on the mass ratio. These values are a bit smaller than the standard Paczyński radius of an accretion disc for this mass ratio range (i.e. $\beta = 0.7$ –0.86, Paczyński 1977). This would indicate that only a portion of the disc is warped out, which could

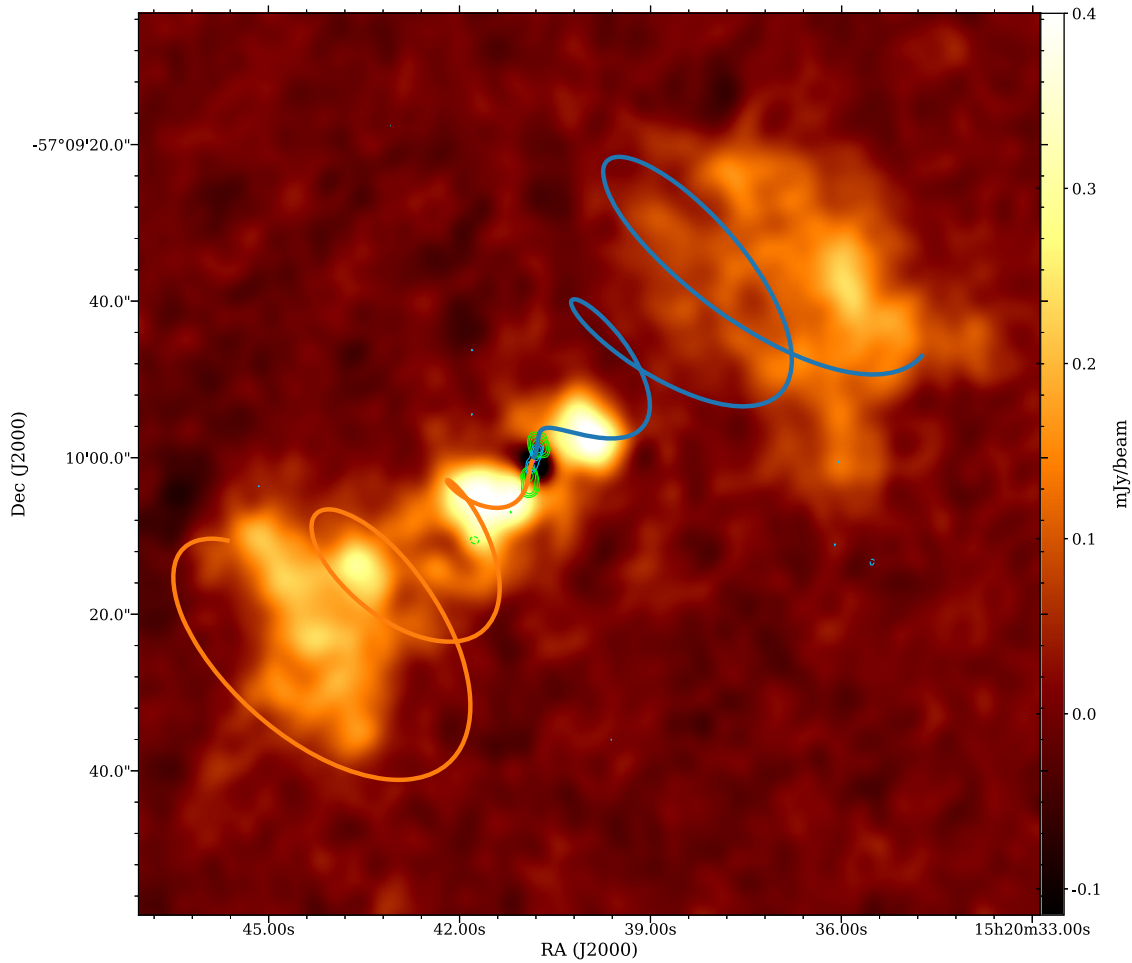


Figure 10. Precessing jet model overlaid on the 2.1-GHz image and the 5.5-, 9.0-, and 34-GHz contours. Only the data within the central 20 arcsec were used for fitting (see Fig. 9). We here show the extrapolation of the model up to the distances of the lobes to verify consistency of the model with the orientations and angular sizes of the lobes. The approaching jet (North-West) is represented in blue and the receding jet (South-East) in orange. Note that ‘approaching’ and ‘receding’ refers here to the orientation of the jet precession axis w.r.t. the line of sight. However, this axis is oriented at 86° to the line of sight and given the half-opening angle of 31° of the precession cone, each jet component will switch from approaching to receding, and vice versa, every precession cycle.

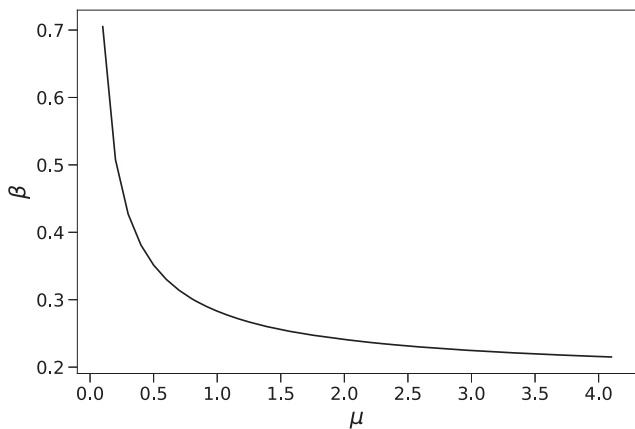


Figure 11. Expected accretion disc outer radius (given as a fraction β of the Roche lobe radius) as a function of the mass ratio μ in the hypothesis that precession of the accretion disc is induced by tidal interactions with the companion star. See equation (4) and text in Section 3.3 for details.

be expected since matter should initially flow from the companion with an angular momentum aligned with the binary orbit. We can conclude that tidal precession is a plausible mechanism to explain our long precession period although the above calculations assume a circular orbit. The significant eccentricity of Cir X-1 orbit should be properly taken into account to derive meaningful values of the warped accretion disc size.

Two additional mechanisms are commonly invoked to explain warping and precession in accretion discs, namely, radiation-driven (Maloney, Begelman & Pringle 1996; Pringle 1996, 1997; Maloney, Begelman & Nowak 1998) and magnetically driven precession (Lipunov & Shakura 1980; Lai 1999, 2003; Terquem & Papaloizou 2000). However, these two mechanisms rely on a significant number of unconstrained parameters related to the microphysics of the accretion disc and/or the magnetic field topology and intensity. This lack of knowledge leads to the estimated precession periods ranging from 10^{-4} to 10^5 yr in the case of NSXBs (see Caproni et al. 2006). In this context, a 5-yr precession period does not seem unreasonable.

Tidal, radiatively driven, and magnetically driven precessions therefore appear as possible mechanisms to explain our results and

deserve further investigations to conclude on their applicability to Cir X-1.

3.4 Orientation of the system

Regarding the inclination of the jet precession axis w.r.t. the line of sight, we note that the value of 86° that the model predicts is not consistent with the upper limit on the jet viewing angle of $\lesssim 5^\circ$ reported by Fender et al. (2004) based on high Lorentz factors inferred from the time delay between radio core flaring and re-brightening of the downstream material in 2000 October. Aside from this inconsistency with the fitted parameter (which might be due to wrong assumptions and/or wrong modelling on our side), for such a low inclination to be compatible with the jet flux ratio, the actual velocity of the jet components must be $\lesssim 0.1c$. Such a low velocity would be in turn inconsistent with the proper motions of 16 and 35 mas d $^{-1}$ observed by Miller-Jones et al. (2012). It is therefore difficult to reconcile the properties of the system inferred from observations in 2000 with the properties of the jets observed in 2010 and 2011. A possibility would be that the system underwent a significant shift in orientation. Modelling of W50's structure (Goodall, Alouani-Bibi & Blundell 2011) has shown that it required at least three distinct epochs of outflows from SS433, each with different properties (such as precession angle) to produce the visible structure, rather than any one stable configuration. Thus, a significant shift in Cir X-1's outflow properties is not a radical concept.

Another possibility would be that the downstream lobe flare observed in 2000 October 21 is in fact associated with a core flare from an earlier periastron passage than the one immediately before. We can check if our model parameters are consistent with this hypothesis. Let us first extend our precession model backward in time as we did to compare with Miller-Jones et al. (2012) observations. On 2000 October 21 and at a distance of 2.3 arcsec from the core, the model predicts a position angle of $136 \pm 25^\circ$ and a North-to-South jet flux ratio of 0.18 ± 0.12 . From coordinates and flux densities given in Tudose et al. (2008), the observed jet position angle is $114 \pm 10^\circ$ and the jet flux ratio 0.16 ± 0.03 therefore broadly consistent with the model predictions. Assuming that our modelling is correct, we derive an instantaneous inclination of the jets w.r.t. the line of sight of 56° . For such an inclination, the time needed for a shell of matter or a shock to travel 2.3 arcsec at $0.5c$ at a distance of 9.4 kpc is 216 d, which corresponds to 13 orbital periods. Taking now into account the uncertainty on the velocity and distance, we obtain a range of travel time from 8 to 24 orbital periods. Given this rather large range, it is difficult to conclude on this possible interpretation. Again, here further investigations and a more precise modelling would be needed.

Another orientation-related remark is that the combination of the inclination i of the system w.r.t. the line of sight and the opening angle ψ of the precession cone implies that at different times, one side of the jet will be approaching or receding, which may explain the shift in north:south jet brightness ratios reported by Calvelo et al. (2012a).

3.5 Core variability

For the data reduction presented in Section 2.2, we introduced a differential gain term into the measurement equation to absorb the potential variability of the unresolved emission from the binary core during the course of the observation.

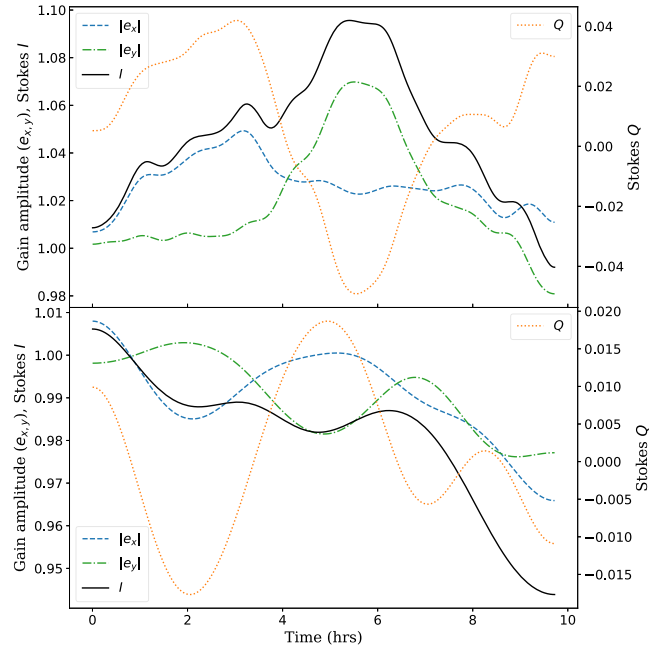


Figure 12. Differential gain-amplitudes as a function of time computed during the calibration of the 5.5 GHz (top panel) and 9.0 GHz (bottom panel) visibilities (see text in Section 3.5). The dashed blue and dash-dotted green lines represent the gain-amplitudes for the X and Y correlations, respectively. The solid black line corresponds to the apparent Stokes I flux relative to the model flux (i.e. $I_{\text{app}}/I_{\text{mod}}$, see equation 5). The dotted orange line corresponds to the apparent Stokes Q flux relative to the model flux (i.e. $Q_{\text{app}}/I_{\text{mod}}$, see equation 6).

As such, the differential gain-amplitudes encode the light curve of the source since other corrupting effects affecting the entire field should have been taken care of by the global gain solutions. If the target source model is unpolarized (which is our case), with constant flux I_{mod} , and the differential gain solutions are given by a diagonal matrix with $e_x(t)$, $e_y(t)$ on the diagonal (corresponding to the X and Y polarizations of the antennas' receivers), then the apparent Stokes I flux is given by

$$I_{\text{app}} = I_{\text{mod}} \frac{(|e_x|^2 + |e_y|^2)}{2}, \quad (5)$$

and the apparent Stokes Q flux by

$$Q_{\text{app}} = I_{\text{mod}} \frac{(|e_x|^2 - |e_y|^2)}{2}. \quad (6)$$

(we only processed dual-polarized data for this study, so U and V are irrelevant).

Fig. 12 shows the differential gain-amplitudes as a function of time, as well as the apparent I_{app} and Q_{app} fluxes (right axis), relative to the model flux I_{mod} . The solutions were obtained using a common ΔE term for all antennas, using the smooth solution mode, with a Gaussian weighting kernel of 15 and 30 min for the 5.5- and 9.0-GHz data, respectively (a larger kernel was chosen for the 9.0-GHz data set due to lower signal-to-noise ratio). We first note the difference between the I_{app} fluxes at 5.5 and 9.0 GHz. Although the data at these two frequency bands have been acquired simultaneously, the corresponding light curves are not identical. While the 5.5-GHz flux rises and fades during the observation, the 9.0 GHz one shows a general decrease. This could be related to the fact that we are probing different structure sizes at 5.5 and 9.0 GHz and/or by spectral variations of the jets. A second notable

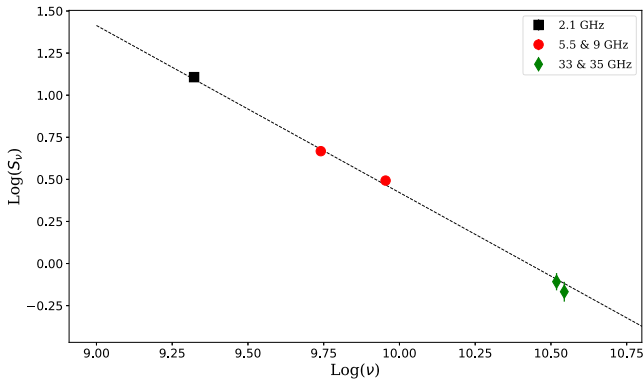


Figure 13. Cir X-1 spectrum of the unresolved core. Flux densities and uncertainties are plotted and obtained from point source fitting to the image plane (see Table 1). Fitting a power law to the data, we derive a spectral index of -0.99 ± 0.02 .

feature appears from these figures. For both frequency bands, we note significant variations of the Q_{app} fluxes that should not be present if the source was unpolarized. Indeed, since the ATCA is an alt-azimuth mount telescope, the X and Y orthogonal feeds of each antennas rotate with respect to the equatorial frame. This causes the actual response of linearly polarized feeds to vary with the angle χ between the ‘sky’ and the feed (which varies with time), according to

$$XX = I + Q \cos(2\chi) + U \sin(2\chi),$$

$$YY = I - Q \cos(2\chi) - U \sin(2\chi).$$

Consequently, given that our source model is unpolarized, if the true source is actually linearly polarized ($Q \neq 0$ and/or $U \neq 0$), the differential gain solutions will correct for these unmodelled variations. Therefore, Q_{app} , as we defined it, should be proportional to $Q \cos(2\chi) + U \sin(2\chi)$, which explains the oscillations we see on Fig. 12. The fact that Cir X-1 emission is polarized is not surprising and consistent with the synchrotron optically thin spectrum we obtain based on our core flux densities measurements (see Fig. 13 and Section 3.6). Finally, we note that the Q_{app} curves at 5.5 and 9.0 GHz are not similar and even seem anticorrelated. The only reasonable explanation that we see is a $\sim 90^\circ (\pm n\pi)$ Faraday rotation induced by the local and/or interstellar medium. Such a rotation angle implies a lower limit on the rotation measure of $\gtrsim 8 \times 10^{-2} \text{cm}^{-2}$ that in turn sets a lower limit on the average of the magnetic field parallel to the line of sight, weighted by the electron density: $n_e B_{\parallel} \gtrsim 10^{-7} \text{Gauss cm}^{-3}$ for a distance of 9.4 kpc.

3.6 Spectrum and nature of the unresolved central outflow

From the point source fitting to the unresolved core, we performed on each data set, we obtain the flux density measurements summarized in Table 1 with the corresponding spectrum shown in Fig. 13. A power-law fit to the data gives a spectral index of -0.99 ± 0.02 , consistent with optically thin synchrotron emission. Note that the steepness of the spectrum is likely accentuated by the presence of jet structures at all scales that are unresolved to the lower frequency beams.

Migliari et al. (2010) have shown that the available spectrum of the atoll-type NSXB 4U 0614 + 091 can be fitted by a flat power law from the radio to the mid-IR implying emission originates in a compact optically thick jet as observed in black hole XRBs in the hard state. However, the jet break frequency, i.e. the frequency at

which the jet becomes transparent to its own synchrotron emission, was lower by a factor of ~ 10 than the one measured in the black hole GX 339–4 during a fully established hard state (Corbel & Fender 2002). Other atoll sources detected in radio have only shown optically thick synchrotron emission consistent with the presence of compact jets (Rutledge et al. 1998; Moore et al. 2000; Migliari et al. 2004; Migliari & Fender 2006; Miller-Jones et al. 2010). Our results indicate that the radio to mm spectrum of Cir X-1 is optically thin during non-flaring periods when, presumably, compact jets could form. This highlights the existing behavioural differences between atoll sources and this neutron star (NS) system. Cir X-1 has shown evidence for discrete jet ejecta moving away from the core following flare events: behaviour that atoll sources lack. If parallels can be made between NS and black hole (BH) systems, then these flares and subsequent ejections should coincide with periods of high accretion on to the NS. Although Cir X-1 is a special case within the standard classification framework, it is believed to have one of the highest accretion rates among the neutron star systems being regularly above the Eddington limit (Heinz et al. 2015). A characteristic shared with Z-sources for which optically thin radio cores are also observed (Migliari 2011). More generally, our results are consistent with the unified picture proposed to explain the different sub-classes of NSXBs as being mainly driven by mass accretion rate (see e.g. Homan et al. 2010; Fridriksson, Homan & Remillard 2015). The weakly accreting atoll sources, producing only compact jets, would be the equivalent of BH in the hard state. When producing jets, the highly accreting NS systems would correspond to the intermediate state (hard-to-soft) BHs displaying mainly transient ejections (see Migliari & Fender 2006; Migliari 2011; and Motta & Fender 2019, for a detailed discussion on jets in NS systems and comparison with BHs).

4 SUMMARY

We have described results of ATCA multifrequency radio observations of the accreting neutron star Circinus X-1. We presented advanced data processing methods that we used to overcome multiple issues due to intrinsic variability of the source and DDEs. We produced what we believe are the most detailed images so far of the jet–signal-to-noise ratio (SNR) interaction in this source, and we think these images could be exploited more, in the future, by groups modelling jet–media interaction.

The centimetre and millimetre radio maps revealed symmetrical jet structures with significant variation of the jet axis angle. We explored the possibility that such a morphology would result from precession by modelling the jet flow path with a kinematic jet model. The result of the modelling suggests that precession is a plausible interpretation and implies that the source displays mildly relativistic jets seen at high inclination with respect to the line of sight. We discussed the incompatibility of our results with previous findings of highly relativistic jets seen at low inclination and concluded that a significant shift of the global orientation of the system might have happened over the last decades.

We then analysed the differential gain solutions obtained during calibration of the centimetre data sets and recovered the intrinsic variability of the source during our observation. Power-law fits to the centimetre and millimetre flux densities of the source then indicated that optically thin synchrotron emission dominates within the extent of the point source regions. The outflowing modes of Cir X-1 thus appear to be dominated by recurrent discrete ejection events in contrast with the compact jet state observed by, e.g. Migliari et al. (2010) in 4U 0614 + 091. This highlights the main differences

between Atoll and Z-type NSXB and is consistent with the unified picture where mass accretion rate is the leading parameter behind the NSXB classification framework.

ACKNOWLEDGEMENTS

We would like to thank the referee for his/her constructive comments that helped in improving the quality of the paper. MC acknowledges the financial assistance of the National Research Foundation (NRF) of South Africa through an SKA SA Fellowship. The ATCA is part of the Australia Telescope funded by the Commonwealth of Australia for operation as a National Facility managed by CSIRO. This research used APLpy, an open-source plotting package for PYTHON (Robitaille & Bressert 2012) and LMFIT, a non-linear optimization package for Python (<https://lmfit.github.io/lmfit-py/>).

REFERENCES

- Armstrong R. P. et al., 2013, *MNRAS*, 433, 1951
 Brandt N., Podsiadlowski P., 1995, *MNRAS*, 274, 461
 Calvelo D. E., Fender R., Broderick J., Moin A., Tingay S., Tzioumis T., Nicolson G., 2010, *Astronomer's Telegram*, 2699, 1
 Calvelo D. E., Fender R. P., Tzioumis A. K., Broderick J. W., 2012b, *MNRAS*, 419, L54
 Calvelo D. E., Fender R. P., Tzioumis A. K., Kawai N., Broderick J. W., Bell M. E., 2012a, *MNRAS*, 419, 436
 Caproni A., Livio M., Abraham Z., Cuesta H. J. M., 2006, *ApJ*, 653, 112
 Casares J., Ribas I., Paredes J. M., Martí J., Allende Prieto C., 2005, *MNRAS*, 360, 1105
 Corbel S., Fender R. P., 2002, *ApJ*, 573, L35
 Eggleton P. P., 1983, *ApJ*, 268, 368
 Eikenberry S. S., Cameron P. B., Fierce B. W., Kull D. M., Dror D. H., Houck J. R., Margon B., 2001, *ApJ*, 561, 1027
 Fender R., Spencer R., Tzioumis T., Wu K., van der Klis M., van Paradijs J., Johnston H., 1998, *ApJ*, 506, L121
 Fender R., Wu K., Johnston H., Tzioumis T., Jonker P., Spencer R., van der Klis M., 2004, *Nature*, 427, 222
 Fender R. P., Kuulkers E., 2001, *MNRAS*, 324, 923
 Fender R. P., Maccarone T. J., van Kesteren Z., 2005, *MNRAS*, 360, 1085
 Fomalont E. B., 1999, in Taylor G. B., Carilli C. L., Perley R. A., eds, ASP Conf. Ser. Vol. 180, *Synthesis Imaging in Radio Astronomy II*. Astron. Soc. Pac., San Francisco, p. 301
 Fridriksson J. K., Homan J., Remillard R. A., 2015, *ApJ*, 809, 52
 Gallo E., Degenaar N., van den Eijnden J., 2018, *MNRAS*, 478, L132
 Geldzahler B. J., Pauls T., Salter C. J., 1980, *A&A*, 84, 237
 Glass I. S., 1978, *MNRAS*, 183, 335
 Goodall P. T., Alouani-Bibi F., Blundell K. M., 2011, *MNRAS*, 414, 2838
 Haynes R. F., Jauncey D. L., Murdin P. G., Goss W. M., Longmore A. J., Simons L. W. J., Milne D. K., Skellern D. J., 1978, *MNRAS*, 185, 661
 Heinz S., Schulz N. S., Brandt W. N., Galloway D. K., 2007, *ApJ*, 663, L93
 Heinz S. et al., 2013, *ApJ*, 779, 171
 Heinz S. et al., 2015, *ApJ*, 806, 265
 Hjellming R. M., Johnston K. J., 1981, *ApJ*, 246, L141
 Homan J. et al., 2010, *ApJ*, 719, 201
 Johnston H. M., Soria R., Gibson J., 2016, *MNRAS*, 456, 347
 Jonker P. G., Nelemans G., Bassa C. G., 2007, *MNRAS*, 374, 999
 Lai D., 1999, *ApJ*, 524, 1030
 Lai D., 2003, *ApJ*, 591, L119
 Larwood J., 1998, *MNRAS*, 299, L32
 Linares M. et al., 2010, *ApJ*, 719, L84
 Lipunov V. M., Shakura N. I., 1980, *Sov. Astron. Lett.*, 6, 14
 Luque-Escamilla P. L., Martí J., Martínez-Aroza J., 2015, *A&A*, 584, A122
 Maloney P. R., Begelman M. C., Nowak M. A., 1998, *ApJ*, 504, 77
 Maloney P. R., Begelman M. C., Pringle J. E., 1996, *ApJ*, 472, 582
 Martin R. G., Tout C. A., Pringle J. E., 2008, *MNRAS*, 387, 188
 Massi M., Zimmermann L., 2010, *A&A*, 515, A82
 Matsuoka M. et al., 2009, *PASJ*, 61, 999
 McMullin J. P., Waters B., Schiebel D., Young W., Golap K., 2007, in Shaw R. A., Hill F., Bell D. J., eds, ASP Conf. Ser. Vol. 376, *Astronomical Data Analysis Software and Systems XVI*. Astron. Soc. Pac., San Francisco, p. 127
 Middelberg E., Sault R. J., Kesteven M. J., 2006, *Publ. Astron. Soc. Aust.*, 23, 147
 Migliari S., 2011, in Romero G. E., Sunyaev R. A., Belloni T., eds, Proc. IAU Symp. 275, *Jets at all Scales*, Cambridge University Press, Cambridge, p. 233
 Migliari S., Fender R. P., 2006, *MNRAS*, 366, 79
 Migliari S., Fender R. P., Rupen M., Wachter S., Jonker P. G., Homan J., van der Klis M., 2004, *MNRAS*, 351, 186
 Migliari S., Fender R. P., van der Klis M., 2005, *MNRAS*, 363, 112
 Migliari S. et al., 2010, *ApJ*, 710, 117
 Miller-Jones J. C. A. et al., 2010, *ApJ*, 716, L109
 Miller-Jones J. C. A. et al., 2012, *MNRAS*, 419, L49
 Mohan N., Rafferty D., 2015, *Astrophysics Source Code Library*, record ascl:1502.007
 Moore C. B., Rutledge R. E., Fox D. W., Guerriero R. A., Lewin W. H. G., Fender R., van Paradijs J., 2000, *ApJ*, 532, 1181
 Motta S.E., Fender R.P., 2019, *MNRAS*, 483, 3686
 Nakajima M. et al., 2010, *Astronomer's Telegram*, 2608, 1
 Nicolson G. D., 2007, *Astronomer's Telegram*, 985, 1
 Nicolson G. D., Feast M. W., Glass I. S., 1980, *MNRAS*, 191, 293
 Noordam J. E., Smirnov O. M., 2010, *A&A*, 524, A61
 Nunhokee C. D., 2015, MSc Thesis, Rhodes Univ., South Africa
 Oosterbroek T., van der Klis M., Kuulkers E., van Paradijs J., Lewin W. H. G., 1995, *A&A*, 297, 141
 Paczynski B., 1977, *ApJ*, 216, 822
 Pringle J. E., 1996, *MNRAS*, 281, 357
 Pringle J. E., 1997, *MNRAS*, 292, 136
 Rajoelimanana A. F., Charles P. A., Udalski A., 2011, *MNRAS*, 413, 1600
 Robitaille T., Bressert E., 2012, *Astrophysics Source Code Library*, record ascl:1208.017
 Rutledge R., Moore C., Fox D., Lewin W., van Paradijs J., 1998, *Astronomer's Telegram*, 8, 1
 Sault R. J., Teuben P. J., Wright M. C. H., 1995, in Shaw R. A., Payne H. E., Hayes J. J. E., ed., ASP Conf. Ser. Vol. 77, *Astronomical Data Analysis Software and Systems IV*. Astron. Soc. Pac., San Francisco, p. 433
 Sell P. H. et al., 2010, *ApJ*, 719, L194
 Shirey R. E., Bradt H. V., Levine A. M., Morgan E. H., 1998, *ApJ*, 506, 374
 Smirnov O. M., 2011, *A&A*, 527, A107
 Smirnov O. M., Tasse C., 2015, *MNRAS*, 449, 2668
 Soleri P., Tudose V., Fender R., van der Klis M., Jonker P. G., 2009b, *MNRAS*, 399, 453
 Soleri P. et al., 2009a, *MNRAS*, 397, L1
 Stewart R. T., Caswell J. L., Haynes R. F., Nelson G. J., 1993, *MNRAS*, 261, 593
 Storn R., Price K., 1997, *J. Glob. Optim.*, 11, 341
 Tasse C., 2014, preprint ([arXiv:1410.8706](https://arxiv.org/abs/1410.8706))
 Tasse C. et al., 2018, *A&A*, 611, A87
 Taylor A. R., Gregory P. C., 1982, *ApJ*, 255, 210
 Tennant A. F., Fabian A. C., Shafer R. A., 1986, *MNRAS*, 219, 871
 Terquem C., Papaloizou J. C. B., 2000, *A&A*, 360, 1031
 Tudose V., Fender R. P., Kaiser C. R., Tzioumis A. K., van der Klis M., Spencer R. E., 2006, *MNRAS*, 372, 417
 Tudose V., Fender R. P., Tzioumis A. K., Spencer R. E., van der Klis M., 2008, *MNRAS*, 390, 447
 Whelan J. A. J. et al., 1977, *MNRAS*, 181, 259

This paper has been typeset from a $\text{\TeX}/\text{\LaTeX}$ file prepared by the author.